Numerical Performance Analysis of a Coandă Aerofoil

Korbinian Stadlberger and Mirko Hornung
Technische Universität München, Lehrstuhl für Luftfahrtsysteme, Germany

Active flow control technology is receiving increased interest for flapless flight control applications. Two modifications of Menter's shear-stress-transport turbulence model are presented and validated aiming to increase robustness and accuracy for the modelling of Coandă flap systems in the preliminary design stages. A large number of Reynolds-averaged Navier-Stokes simulations has been performed for a representative circulation control aerofoil to assess its control moment effectiveness. The final analysis enables statements about the sensitivity of lift and pitching moment generation to geometric parameters and blowing conditions.

Nomenclature

α	=	angle of attack	[deg]
η_h	=	outflow momentum ratio based on slot heights	[-]
$\frac{\partial c_l/\partial \eta_h}{c_\mu}$	=	Coandă flap lift gain efficiency	[-]
$\frac{\partial c_l}{\partial c_\mu}$	=	lift augmentation	[-]
$\frac{\partial c_l}{\partial \eta_h}$	=	Coandă flap lift gain	[-]
$\frac{h}{r}$	=	ratio of slot height to Coandă radius	[-]
$\frac{r}{c_{base}}$	=	ratio of Coandă radius to baseline aerofoil chord	[-]
$\frac{U_{jet}}{U_\infty}$	=	jet outflow velocity ratio	[-]
μ_t	=	eddy viscosity due to turbulence	[Pa s]
μ_{eff}	=	effective viscosity, $\mu_{eff} = \mu + \mu_t$	[Pa s]
ν	=	kinematic viscosity	[m²/s]
ν_t	=	turbulent eddy viscosity	[m²/s]
ω	=	turbulence frequency	[1/s]
ρ	=	air density	[kg/m³]
Θ_{sep}	=	jet separation angle on Coandă surface	[deg]
ε	=	amplification factor	[-]
$\vec{u}$	=	vector of local velocity	[m/s]
A	=	cell surface area	[m²]
c_d	=	drag coefficient based on Coandă aerofoil chord length	[-]
c_l	=	lift coefficient based on Coandă aerofoil chord length	[-]
c_m	=	pitching moment coefficient based on Coandă aerofoil chord length	[-]
c_μ	=	jet outflow momentum flux coefficient, $C_\mu = \frac{U_{jet}\dot{m}_{jet}}{\frac{1}{2}\rho U_\infty^2 S_{ref}}$	[-]
c_{base}	=	chord of unmodified baseline aerofoil	[m]
c_{Coanda}	=	chord of Coandă aerofoil	[m]
D	=	fluid element deformation tensor	[1/s]
d	=	normal distance from wall	[m]
F_D	=	wall jet marker function	[-]
h_l	=	height of lower slot	[m]
h_{total}	=	total slot height, $h_{total} = h_u + h_l$	[m]
h_u	=	height of upper slot	[m]
k	=	turbulent kinetic energy	[m²/s²]
k_s	=	sand-grain height	[m]
p	=	static pressure	[N/m²]
r	=	radius of Coandă surface	[m]
u	=	horizontal velocity component	[m/s]
U_∞	=	free stream velocity	[m/s]
u_τ	=	friction velocity	[m/s]
u_Θ	=	tangential velocity on Coandă surface	[m/s]
U_{jet}	=	mean jet outflow velocity	[m/s]
V	=	cell volume	[m³]
v	=	vertical velocity component	[m/s]
y_{Coanda}	=	normal distance from Coandă surface	[m]

1 INTRODUCTION

Active flow control technology is receiving increased interest for high-lift and flight control applications [1, 2, 3, 4, 5, 6, 7]. While high potential lift coefficients provided by blown flaps contribute to short take-off and landing distances (STOL) the concept of fixed blown trailing edges enables flapless flight control with reduced observability. Military applications may profit from the lower radar scattering of minimised gaps whereas civil implementations of a so called Coandă flap can be beneficial in terms of effectiveness, weight and maintenance cost. In the framework of the national research program SAGITTA a reliable prediction method for system design is sought that estimates aerodynamic data correctly enough for preliminary design stages. In the design process numerous parameter studies demand fast but sufficiently accurate calculation methods to explore the design space. Modelling approaches based on potential theory are inappropriate for the modelling of blown wings as the flow problem is mainly driven by turbulence and

diffusive processes. Since computational capacity has grown exponentially over the last twenty years the automated solution of the Reynold's averaged Navier-Stokes equations (RANS) inside numerous flow simulations appears reasonable also for preliminary design, at least in the two-dimensional case. Once having set up a 2D data set this section data then can be extrapolated easily on a finite wing by a method relying on potential theory [8].

Figure 1 shows an exemplary flowfield of an experimental Coandă aerofoil with round trailing edge under blowing conditions. The internal pressurised air leaves the upper slot with height h_u having a mean velocity U_{jet}. The jet bounds to the wall and mixes with the turbulent boundary layer flow arriving from the upper side of the aerofoil and forms the typical wall jet velocity profile on the Coandă surface (Figure 5). Depending on the jet's turbulence characteristics and counterpressure the wall jet separates at angle Θ_{sep} (Figure 6) and aligns with the free stream. Further turbulent and viscous mixing processes alleviate the over velocities until complete free stream assimilation. As circulation increases with blowing rate a shift of the leading edge stagnation point as well as an intensified suction peak (Figure 3) with possible short separation bubble can be expected. Even at zero angle of attack lift coefficients of 8 and beyond could be measured during wind tunnel experiments [5]. For flight control purposes a double-slotted trailing edge design can act similarly to a conventional flap where the momentum vector is bended both upwards or downwards. In addition, this design promises to be suitable also for yaw control when air outflow momentum is controlled differentially on the wing half spans. If the underlying RANS model yields robust and sufficiently accurate results for the attainable aerodynamic forces and moments of the Coandă aerofoil the calculated section data thereafter can be used to evaluate the flow control system for a given finite wing [8].

Whereas some modelling efforts indicate a certain success in using RANS to predict trends and selected details [9] there have been more failures of RANS models than successes [10, 11, 12, 13, 14]. Failures typically manifest themselves in a wall jet which stays attached too long on the Coandă surface. In the first instance this leads to an excessive overprediction of the lift coefficient but then turns into a gross underprediction when the jet wraps around (Figure 2) and deteriorates the lower side pressure distribution (Figure 4). The turbulence model used for RANS closure is decisive for the final result, as the eddy viscosity predictions inside the wall jet determine the location of jet separation. Unfortunately a distinct all-embracing statement about the most appropriate turbulence model for circulation control is not possible if one has to give a final conclusion of available literature at present. The author finally chose Menter's SST turbulence model [15] to be implemented in the RANS model. During first studies the same jet-wrap-around phenomenon was encountered and promptly revealed as crucial instability that invalidated the first attempts to analyse the performance of a Coandă aerofoil systematically [14]. Therefore the main objective of subsequent studies was to increase both robustness and predictability of steady RANS simulations within the scope of Coandă flap system design. In the end two turbulence model modifications have been developed for the adjustment of Menter's SST turbulence model [15] in order to stabilise large automated calculation campaigns.

The following article provides the mathematical formulation behind the developed RANS tool including the baseline turbulence model and gives a short characterisation of the numerical methods used for the implementation in the Matlab environment. The subsequent section then describes the two modifications of the original turbulence model which thereafter are assessed on the Englar/Jones test case [5]. Finally the presented method is applied inside the parametric study of a more practical circulation control version of the NACA-64A012 aerofoil. At last the calculated results and sensitivities are discussed before final statements conclude this article.

2 MATHEMATICAL AND NUMERICAL FORMULATION

For the estimation of attainable steady forces and moments in the two-dimensional case the Reynolds Averaged Navier-Stokes equations are processed inside the Matlab environment from Mathworks. To reduce computational efforts and to increase robustness the fluid of the given flow problem is considered as an incompressible Newtonian fluid. Past numerical studies have shown negligible influence of compressibility up to jet exit velocities close to $Ma = 1$ [16]. According to the finite volume method the incompressible momentum equations for a velocity component u_i in cartesian coordinates can be written in the following integral form by using Gauss's divergence theorem

$$\int_{CV} \frac{\partial (u_i)}{\partial t} dV + \int_{A} \vec{n} \cdot \left(u_i \cdot \vec{u} \right) dA = - \int_{CV} S_{p_i} dV + \int_{A} \vec{n} \cdot \left(\mu_{eff} \operatorname{grad} u_i \right) dA + \int_{CV} S_{u_i} dV \quad (1)$$

where $S_{p_i} = \frac{\partial p}{\partial x_i}$ constitutes the pressure source term and S_{u_i} an arbitrary momentum source term. The normal vectors on the control volume's (CV) boundary surfaces A are denoted by $\vec{n}$.

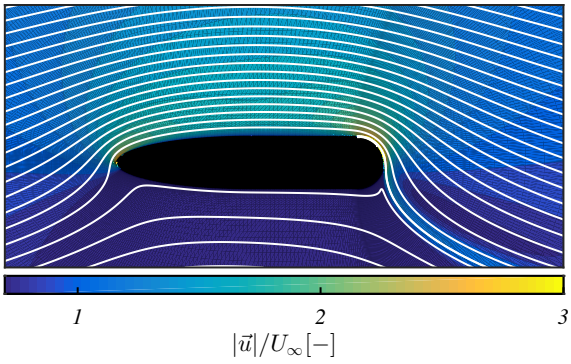

Fig. 1. Illustration of flow field due to blowing

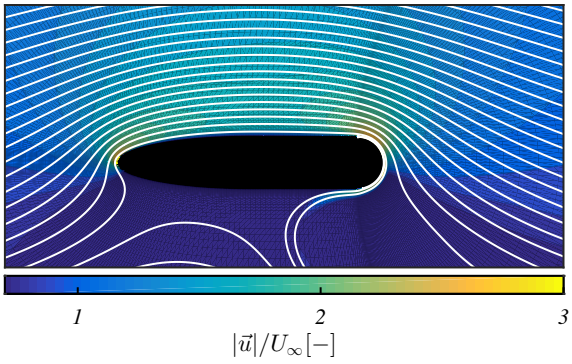

Fig. 2. Flow field exhibiting jet-wrap-around phenomenon

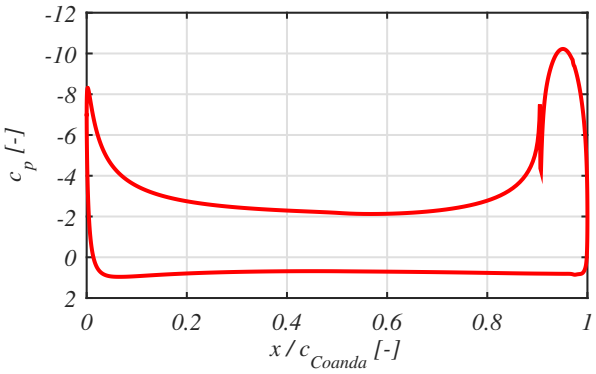

Fig. 3. Pressure distribution of Coandă aerofoil

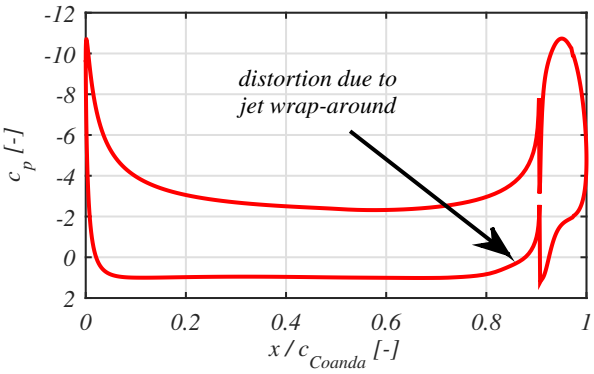

Fig. 4. Pressure distribution in case of jet-wrap-around

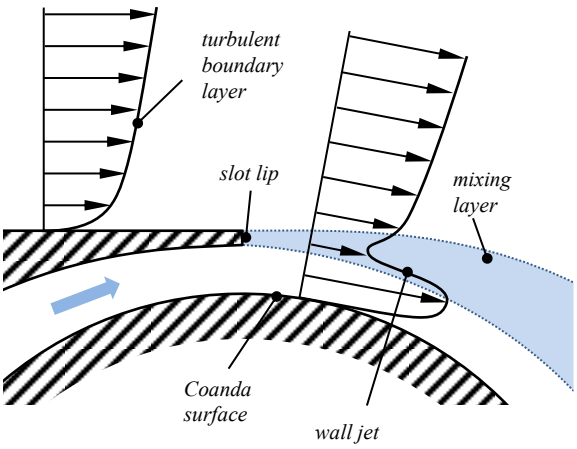

Fig. 5. Illustration of wall jet near slot

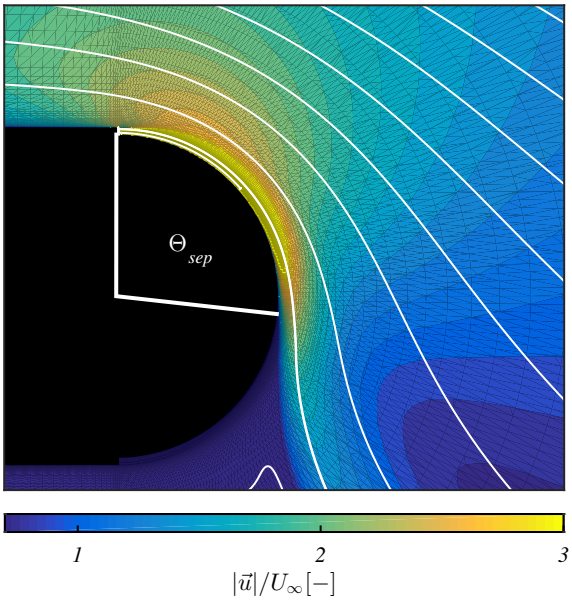

Fig. 6. Detailed illustration of jet separation at the trailing edge

The continuity equation is given by

$$\int_{CV} \frac{\partial \rho}{\partial t} dV + \int_{A} \vec{n} \cdot \vec{u} \, dA = 0 \tag{2}$$

The current implementation of the steady solver omits transient terms $\int_{CV} \frac{\partial \Phi}{\partial t} dV$ and is based on the hybrid differencing scheme which combines both upwind and central differencing schemes [17]. Depending on the local Peclet number the second-order accurate central differencing scheme or the unconditionally stable upwind differencing scheme is employed which prevents numerical instabilities due to coarse discretisation. To avoid a non-physical "checker-board" pressure field a staggered grid approach for velocity components and scalar parameters has been implemented [18]. Finally, a coupled solver strategy with a combined system of linear equations has been established which solves the momentum and continuity equations simultaneously.

For closure of the RANS equations Menter's k-ω-models (BSL/SST) [19, 15] were selected to estimate the extra turbulent stress terms (in 2D: $\overline{u'^2}$, $\overline{v'^2}$, $\overline{u'v'}$) evolving from time-averaged turbulent velocity fluctuations. The steady state, incompressible formulation consists of two transport equations. The turbulent kinetic energy k is given by

$$\operatorname{div}\left(k\vec{u}\right) = \operatorname{div}\left[\left(\nu + \sigma_k \nu_t\right) \operatorname{grad} k\right] + \left(\nu P\right)_k - \beta^* k\omega \tag{3}$$

with the production term $P = 2\left[\left(\frac{\partial u}{\partial x}\right)^2 + \frac{1}{2}\left(\frac{\partial u}{\partial y} + \frac{\partial v}{\partial x}\right)^2 + \left(\frac{\partial v}{\partial y}\right)^2\right]$.

The turbulence frequency ω is given by

$$\operatorname{div}\left(\omega\vec{u}\right) = \operatorname{div}\left[\left(\nu + \sigma_\omega \nu_t\right) \operatorname{grad} \omega\right] + \gamma P - \beta\omega^2 + \\ + 2\left(1 - F_1\right) \frac{\sigma_\omega}{\omega} \left(\frac{\partial k}{\partial x}\frac{\partial \omega}{\partial x} + \frac{\partial k}{\partial y}\frac{\partial \omega}{\partial y}\right) \tag{4}$$

where the blending function F_1 is defined by

$$F_1 = \tanh\left\{\left\{\min\left[\max\left(\frac{\sqrt{k}}{\beta^*\omega d}, \frac{500\nu}{d^2\omega}\right), \frac{4\rho\sigma_\omega k}{CD_{k\omega} d^2}\right]\right\}^4\right\} \tag{5}$$

with $CD_{k\omega} = max\left(2\rho\frac{\sigma_\omega}{\omega}\left(\frac{\partial k}{\partial x}\frac{\partial w}{\partial x} + \frac{\partial k}{\partial y}\frac{\partial w}{\partial y}\right), 10^{-10}\right)$ and d as the distance to the nearest wall. F_1 is equal to zero away from the surface (k-ε-model) and switches over to one inside the boundary layer (k-ω-model). The constants of the model are blended accordingly using $c_i = F_1 c_{k-\omega} + \left(1 - F_1\right) c_{k-\varepsilon}$ whose original coefficients for the BSL model are given in Table 1.

To prevent the build-up of turbulence in stagnation regions the production term of turbulent kinetic energy $\left(\nu P\right)_k$ is limited using

$$\left(\nu P\right)_k = min\left(\left(\nu P\right)_k, 10\beta^*\rho k\omega\right) \tag{6}$$

Table 1. Turbulence model coefficients of Menter's BSL model

coefficient	k-ω-model ($F_1 = 1$)	k-ε-model ($F_1 = 0$)
σ_k	0.5	1
σ_ω	0.5	0.856
β	3/40	0.0828
β^*	0.09	0.09
γ	5/9	0.44

.

For the baseline model (BSL) the turbulent eddy viscosity finally yields

$$\nu_t = \frac{k}{\omega} \tag{7}$$

For the shear-stress-transport-model (SST) the constant coefficient σ_k changes to 0.85 and the eddy viscosity is limited by the following expression

$$\nu_t = \frac{a_1 k}{max\left(a_1\omega, \sqrt{P}F_2\right)} \tag{8}$$

where F_2 is a second blending function which is defined as

$$F_2 = \tanh\left[\max\left(\frac{2\sqrt{k}}{\beta^*\omega d}, \frac{500\nu}{d^2\omega}\right)^2\right] \tag{9}$$

The boundary condition for the turbulent kinetic energy k for no-slip walls is $(k)_{wall} = 0$. For ω the boundary condition values are calculated according to Hellsten [20] and yield

$$(\omega)_{wall} = \frac{u_\tau^2}{\nu} S_R \tag{10}$$

where u_τ is the friction velocity $u_\tau = \sqrt{\tau_w/\rho}$ and S_R is a non-dimensional function defined as

$$S_R = \begin{cases} \left(50/\max\left(k_s^+, k_{s,min}^+\right)\right)^2 & for\, k_s^+ < 25 \\ 100/k_s^+ & for\, k_s^+ \geq 25 \end{cases} \tag{11}$$

Here k_s^+ is the non-dimensional sand-grain height $k_s^+ = u_\tau k_s/\nu$ that is limited from below to a value of $k_{s,min}^+ = 2.4\left(y^+\right)_{wall}^{0.85}$ for ideally smooth surfaces and depends on the non-dimensional thickness $\left(y^+\right)_{wall}$ of the first computational cell adjacent to the wall.

3 TURBULENCE MODEL MODIFICATIONS

Initial test calculations with high jet outflow ratios $\frac{U_{jet}}{U_\infty}$ led to results deteriorated by the aforementioned jet-wrap-around phenomenon where the jet remains attached to the Coandă surface too long, even wraps around and shifts the rear stagnation point to the lower side of the aerofoil up to a non-physical extent

(Figure 2). The reasons are associated with the eddy viscosity prediction inside the characteristic wall jet velocity profile (Figure 5). The following subsections propose two modifications and corrections for the baseline turbulence model which proved to alleviate the encountered problems in terms of accuracy and convergence robustness at higher blowing rates.

3.1 Wall Jet Correction (WJC)

First results indicate that Menter's blending function (eq. 5) is inconvenient for the treatment of fluid over-speeds near the wall, e.g. wall jets. The jet sheet is partly modeled by the k-ε-model even in regions close to the wall where the k-ω-model should dominate. For boundary layer flows near walls, and especially for separating flows in adverse pressure gradient, the k-ω-model is superior to the k-ε-model in terms of accuracy where the latter is prone to the wrong prediction of delayed separation [19]. To mark the entire wall jet zone to be treated by the k-ω-model the following expression provided robust results in the scope of the tested cases.

$$F_D = \tanh\left[\left(\varepsilon \cdot \frac{D\nu}{U_\infty^2}\right)^3\right] \tag{12}$$

where D is the norm of the fluid element deformation tensor yielding $D = \sqrt{\frac{\partial u_i}{\partial x_j}\frac{\partial u_j}{\partial x_j}}$. This ensures that the mixing layer is selected ($F_D \approx 1$) due to its strong velocity gradients relative to the free stream velocity U_∞. The amplification factor ε was calibrated from numerical experiments and was set to the value of $1 \cdot 10^4$ for the present calculations. This wall jet marker function was introduced into equation 5 which then yields

$$F_1 = \tanh\left\{\left\{\min\left[\max\left(\frac{\sqrt{k}}{\beta^* \omega d}, \frac{500\nu}{d^2\omega} + F_D\right), \frac{f_{SG}\rho\sigma_\omega k}{CD_{k\omega}d^2}\right]\right\}^4\right\} \tag{13}$$

Note that the factor f_{SG} inside the safeguard term had to be increased from 4 to 40,000 to correct its erroneous behavior inside the wall jet.

3.2 Modification of SST-Model Formulation (SSTMod)

The application of the original shear-stress-transport model (SST) leads to reduced eddy viscosities in the mixing layers of the downstream wall jet near the slot lip. The extraordinarily high strain rates in the lip wake make equation (8) act like an eddy viscosity limiter in the mixing layer region. Therein too low eddy viscosity values prevent the wall jet from momentum diffusion into the aerofoil free stream. The wall jet can preserve its overspeed up to non-physical distances and detaches too late or even not at all. Therefore a modified formulation of F_2 is proposed to deactivate the eddy viscosity limitation due to SST in the mixing layer regions of the wall jet. Equation (8) is extended by F_D (eq. 12) and yields

$$\nu_t = \frac{a_1 k}{max\left(a_1\omega,\ \sqrt{P}\,(F_2 - F_D)\right)} \tag{14}$$

4 VALIDATION

The present method and its turbulence model modifications are validated by modelling Englar and Jones' wind tunnel experiments from ref. [5]. The aerofoil geometry and used grid topology are given in Figure 7. For the subsequent numerical studies the domain was modelled by a total longitudinal point number of about 500 around the entire surface with approx. 180 of these points concentrated on the Coandă trailing edge. The grid section covering the wall jets contained approx. 90 points in the normal direction to the surface where the total number of grid points was about 100,000 for the investigated mesh. The normal grid spacing inside the boundary layers was resolved such that the first nodes adjacent to the wall fulfil the requirement $y^+ < 1$. The internal plenum was not modelled in this study. Instead, the jet inflow boundary conditions were set directly at the vertical slot boundary below the slot lip. The jet inflow velocity profile was approximated by a simple polynomial function of degree 10. Test calculations indicated insignificant dependence on the degree. Inflow turbulence parameters k and ω at the slot exit were set to laminar flow conditions. The measured slot exit velocity profile indicates that the strong acceleration of the fluid inside the nozzle leads to relaminarised turbulence conditions in this zone [5]. The sand-grain height was set to $k_s = 0.05mm$ for wall boundaries on the entire aerofoil including the Coandă surface. In some references turbulence models with implemented flow curvature correction (e.g. Hellsten [20], [21]) tend to alleviate the problem of non-physical solutions at high blowing rates but give no general guarantee [22, 11, 10, 16]. Note that curvature corrections have not been activated during this study since initial calculations with Hellsten's correction revealed a volatile behaviour and mostly led to erratic results. According to the wind tunnel experiments the free stream velocity U_∞ was set to low subsonic conditions yielding a Reynold's number of $500,000$. The calculated values for the mean jet outflow velocity ratio $\frac{U_{jet}}{U_\infty}$ ranged from 0 to 10. In literature it is common to describe the aerodynamic force and moment reactions dependent on the normalised momentum flux of the outflow, i.e. the equivalent thrust force. The flow momentum coefficient c_μ therefore yields

$$c_\mu = \frac{\dot{m}_{jet} U_{jet}}{\frac{1}{2}\rho_\infty U_\infty^2 S_{ref}} \tag{15}$$

Coandă aerofoil from Englar/Jones, 2009	
t/c	20%
camber	0%
r/c	0.095
$c\,[m]$	0.22
Re	$\backsim 500,000$
$h_u\,[mm]$	0.23, 0.33, 0.46, 0.66, 1.09
$h_{lip}\,[mm]$	0.25

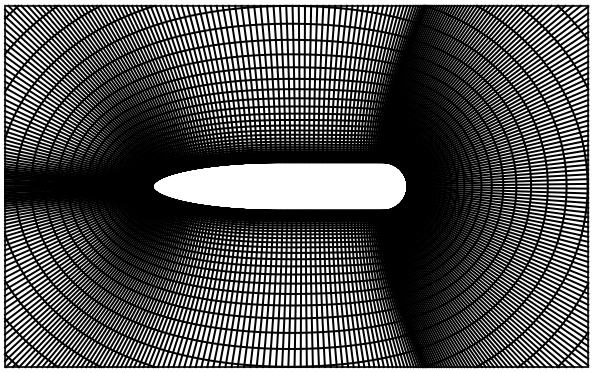

Fig. 7. Circulation control aerofoil geometry and grid topology

where $\dot{m}_{jet}$ is the jet mass flow, U_{jet} the jet outflow velocity, $\frac{1}{2}\rho_\infty U_\infty^2$ the free stream dynamic pressure and S_{ref} the lifting surface reference area.

The calculations in the scope of this study were performed on in-house desktop machines equipped with Intel Core i7-4770 processors (quad core, 3.40Ghz) and 8GB RAM. One iteration took between 5s and 10s where convergence was attained after 40 to 80 iterations in the majority of cases. The convergence criterion was based on the fluctuation and evolution of the lift coefficient.

The following paragraphs describe the impact of the turbulence model modifications on the lift generation c_l as well as on the implied wall jet profiles. Figure 8a shows the section lift c_l over the blowing momentum flux coefficient c_μ. For low to moderate blowing rates the BSL and SST lift increment curves exhibit a similar curve slope as the experimental data until they suddenly drop to a lower level. Figure 8b reveals that the simulations are corrupted by the well-known jet-wrap-around phenomenon indicated by $\Theta_{sep} > 170°$.

By introducing the wall jet correction (WJC) jet-wrap-around can be delayed up to very high blowing rates and, despite a general underprediction, lift results compare essentially well with experimental data. As described in section 3.1 this modification of the blending function formulation aims to retain the use of the k-ω-model throughout the entire wall jet. A more detailed wall jet examination reveals that, compared to the BSL model, the jet velocity peaks with activated WJC attenuate visibly along the Coandă surface (see Figure 9a). The modified blending function F_1 triggers the k-ω-model throughout the entire wall jet profile (Figure 9c) and leads to significantly higher eddy viscosity values in the mixing layer (Figure 9b). This enhances momentum transport towards free stream and prevents the wall jet from jet-wrap-around at higher blowing rates.

The modification of the SST formulation (SSTMod) aims to deactivate its original turbulence limiting behaviour inside the wall jet regions but tries to preserve its well established function in the remaining flow domain including standard boundary layers under adverse pressure gradients. As can be seen in Figure 10c the marker function identifies the wall jet zone and deactivates the SST limiter in these regions as given by the term $F_2 - F_D$ in eq. 3.2. The velocity profiles with modified SST formulation (SSTMod) exhibit an almost identical shape as the baseline model (BSL) even if eddy viscosity values differ significantly and still retain a volatile behaviour (Figure 10b). Note that WJC is not activated in this comparison and jet-wrap-around still occurs at higher blowing rates (Figure 8).

Finally, the two modifications were activated simultaneously in addition to Menter's SST-model which gave the most robust results up to very high blowing rates (Figure 8). These settings then were applied for additional slot heights. The results of the presented RANS method were compared with wind tunnel data and, additionally for $h_u = 0.3mm$, with numerical results calculated with the commercial solver Ansys CFX. The latter rely on a grid consisting of approximately $1.1 \cdot 10^6$ elements which also includes a mesh block representing the geometry of the internal plenum. Inside the CFX preprocessor Menter's original SST model was selected for turbulence modelling. As can be seen in Figure 11 both solvers are able to predict the generated lift quite accurately in the regime of low blowing rates. However, at moderate and high blowing conditions the numerical results deviate significantly from wind tunnel measurements. The author's solver reveals more conservative and underrates the Coandă flap effectiveness. In contrast, the CFX solver overestimates the lift increase even with activated curvature correction (RCC) [21] which, at least, could prevent the jet-wrap-around phenomenon. Further calculations with solely the author's method led to results for additional slot sizes as depicted in Figure 11b. The predicted values agree quite well with experimental data for larger slot sizes up to moderate blowing rates. However, the reduced lift generation for the smallest slot height could not be reproduced numerically. Again, for all slot sizes the results exhibit

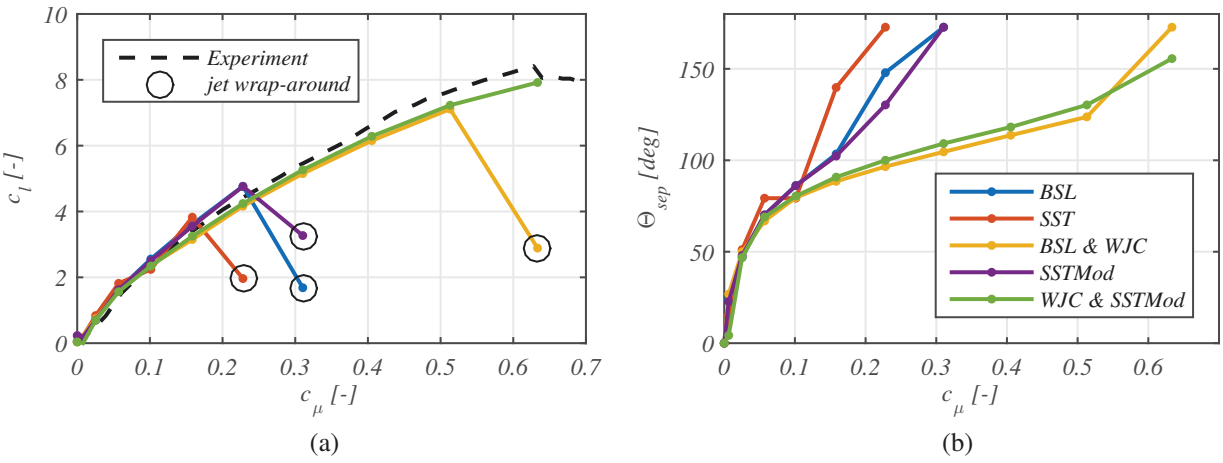

Fig. 8. Lift coefficient increment (a) and wall jet separation angle (b) with turbulence model modifications activated individually, $h_u = 0.5mm$, $\alpha = 0°$

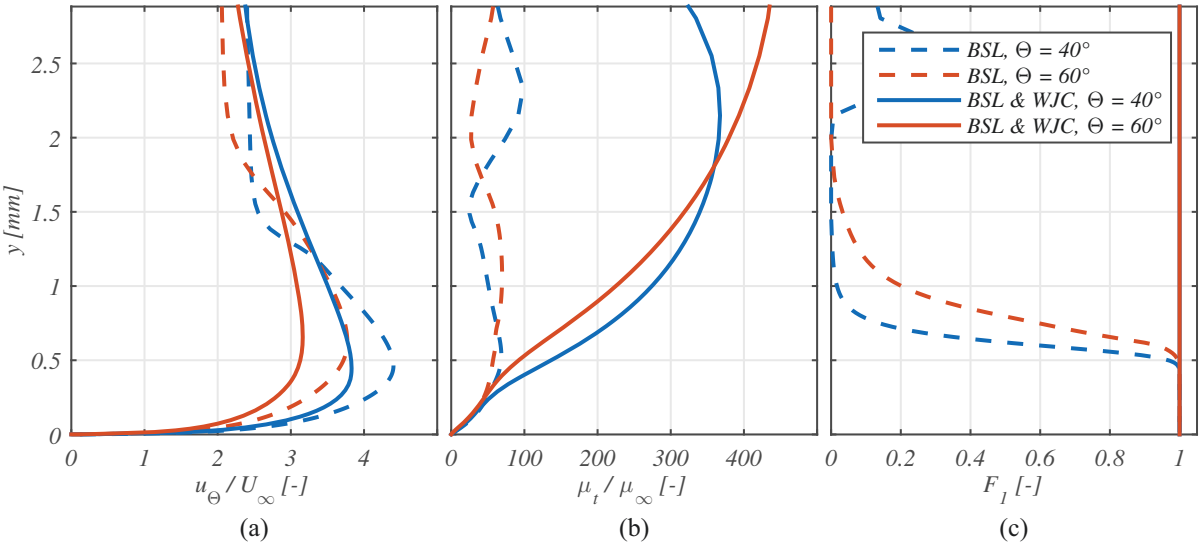

Fig. 9. Velocity (a), eddy viscosity (b) and blending function (c) of wall jet with activated WJC, $\frac{U_{jet}}{U_\infty} = 5$, $c_\mu = 0.158$, $h_u = 0.5mm$, $\alpha = 0°$

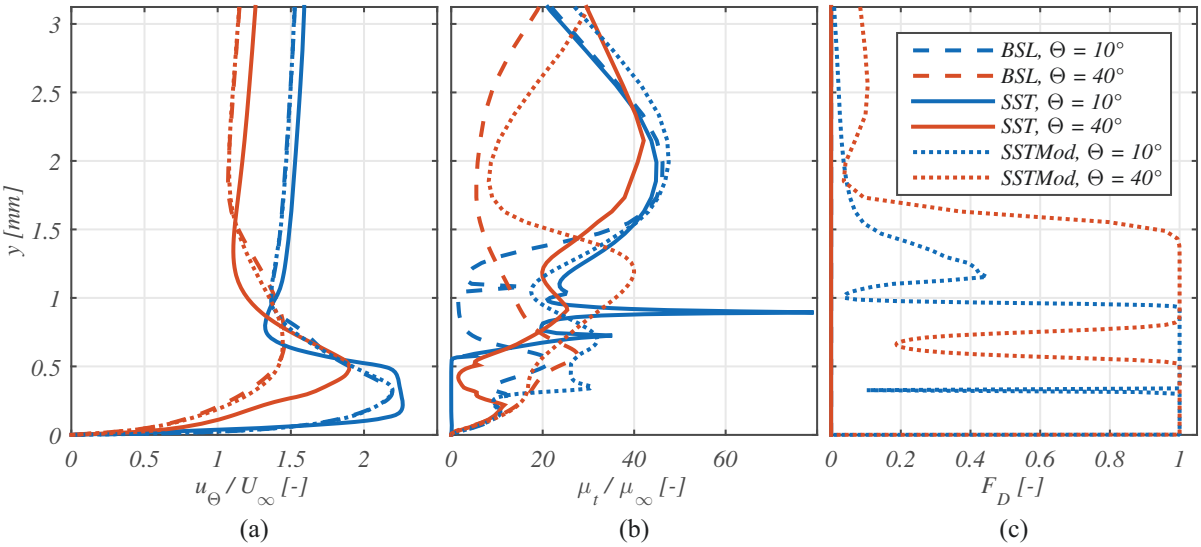

Fig. 10. Velocity (a), eddy viscosity (b) and SST modification function (c) of wall jet with modified SST formulation, $\frac{U_{jet}}{U_\infty} = 2$, $c_\mu = 0.025$, $h_u = 0.5mm$, $\alpha = 0°$

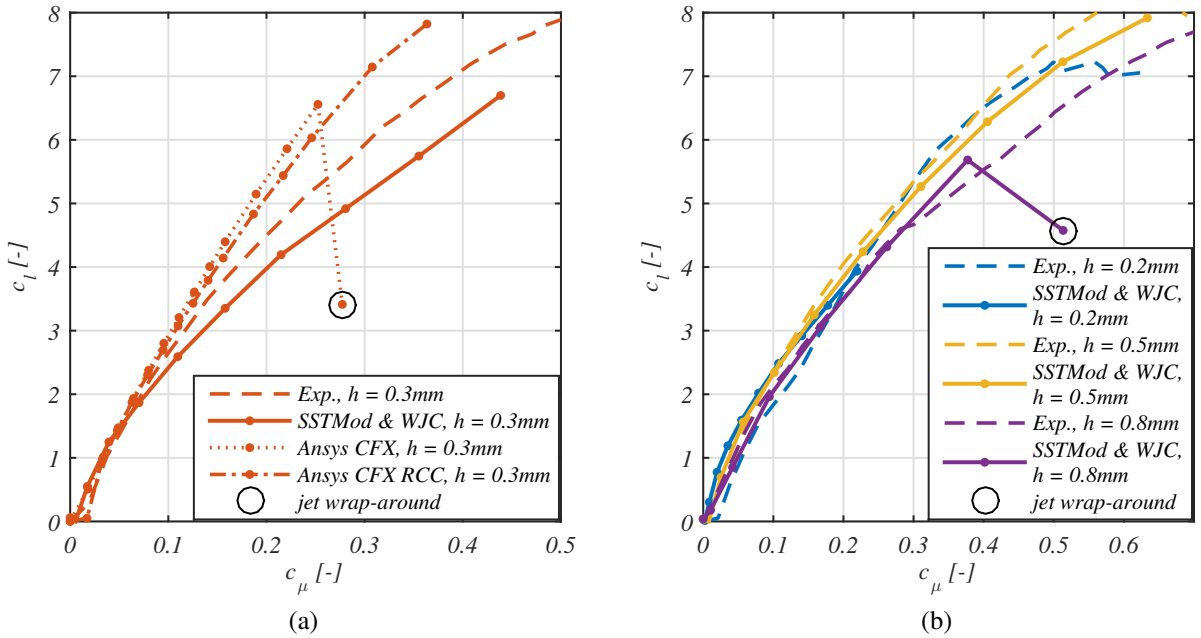

Fig. 11. Lift generation of the Englar/Jones test case [5] due to blowing for different slot heights, $\alpha = 0°$

a visible discrepancy at high blowing rates where jet-wrap-around could not be avoided for the largest tested slot height. Note that wind tunnel data for active flow control aerofoils generally imply several uncertainties. The generation of high lift coefficients leads to significant three-dimensional effects inside the wind tunnel that can affect the effective angle of attack along span. Additionally, varying total pressure losses due to viscous effects inside the internal ducts as well as differing slot heights at the jet exit due to non-uniform bending loads on the rear skin fractions influence the local outflow velocity and mass flow rate [4, 5]. Thus, the real flow momentum coefficient may vary from the total value at the spanwise location where the pressure sensors are installed for lift force integration. Moreover during experiments the total c_μ- value is typically determined through total mass flow measurement inside the supply duct and jet exit velocities that are estimated analytically. Under the assumption of isentropic flow the pressure ratio of total pressure inside the plenum and free stream static pressure are used for the calculation of the jet outflow Mach number. So the experimental c_μ-value is prone to errors resulting from real local static pressures at the slot exit that differ from the free stream value. Especially when high lift increments are attained the experimental c_μ- values tend to be underrated significantly.

5 APPLICATION AND PERFORMANCE ANALYSIS

The previously presented and validated calculation method with modified turbulence model is applied on the NACA64A012CC aerofoil whose geometry data are given in Figure 12. In this calculation campaign the used grid had a total longitudinal point number of about 350 around the entire surface with approximately 70 to 100 of these points concentrated on the Coandă trailing edge. The grid sections covering the wall jets had approximately 90 points in the normal direction to the Coandă surface giving a total number of grid points of about 70,000 for each of the investigated meshes. The calculations were performed on the same machines as in section 4. One iteration took between 4s and 6s where a converged lift coefficient was attained after an average number of 60 iterations. Several parameter variations (e.g. Coandă radius r, slot heights h_u and h_l, blowing velocity $\frac{U_{jet}}{U_\infty}$etc.) have been investigated during the completely automated calculation campaign on 18 quad-core desktop machines enabling a total number of 72 simultaneous simulations. Finally, the results of 30,000 calculated data points are available for performance analysis. In contrast to the previous validation case (section 4) the concept of the present circulation control aerofoil features both an upper and lower slot. These are supplied by one common plenum chamber imposing one total pressure value. Thus, the momentum flux coefficients $(C_\mu)_{upper}$ and $(C_\mu)_{lower}$ of the upper and lower slot can be controlled by adjusting their respective slot heights as the outflow velocity U_{jet} is solely defined by the total pressure inside the plenum. For the following analysis of the numerical results a new control parameter η_μ is defined as follows

$$\eta_\mu = \frac{(C_\mu)_{upper} - (C_\mu)_{lower}}{(C_\mu)_{upper} + (C_\mu)_{lower}} \tag{16}$$

This relative outflow momentum ratio is meant to be

NACA 64A012CC	
t/c	12%
camber	0%
$c_{base}\,[m]$	1
r/c_{base}	$0.01 - 0.04$
Re	$\backsim 4,000,000$
$h_{u/l}\,[mm]$	$0.1 - 1.9$
$h_{lip}\,[mm]$	0.5

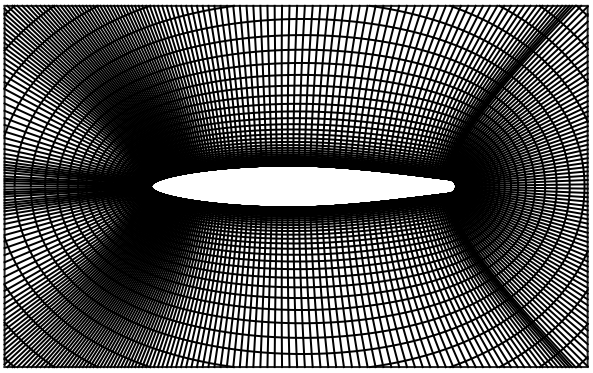

Fig. 12. NACA 64A012 circulation control aerofoil geometry and grid topology

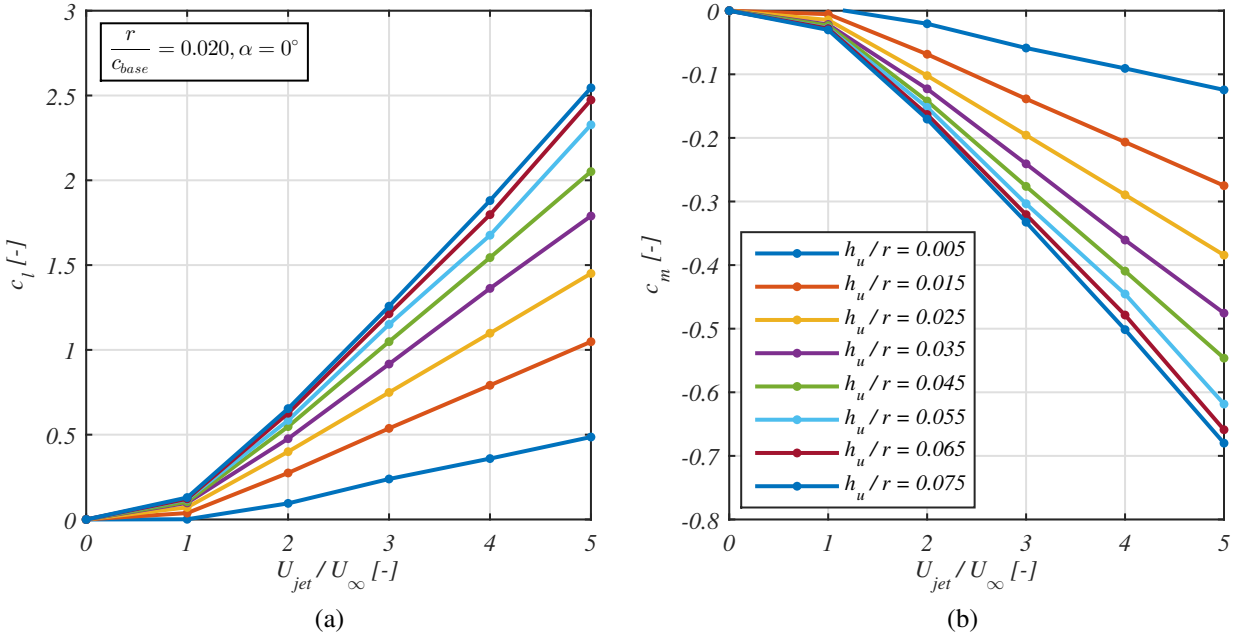

Fig. 13. Lift (a) and pitching moment (b) due to blowing through upper slot over jet velocity ratio ($\eta_h = 1$)

equivalent to a plain flap deflection ranging from -1 (flap deflected 100% upwards) to 1 (flap deflected 100% downwards) and can be approximated by the following expression

$$\eta_\mu \approx \eta_h = \frac{h_u - h_l}{h_{total}} \tag{17}$$

where $h_{total} = h_u + h_l$ is the sum of upper and lower slot height h_u and h_l, respectively. Again, the control parameter η_h spans the operational range from the cases of completely closed upper slot ($h_l = h_{total}$; $\eta_h = -1$) to completely closed lower slot ($h_u = h_{total}$; $\eta_h = 1$).

Maximum Effectiveness ($\eta_h = 1$): For the present concept maximum control effectiveness is expected to be attained through single-slot-blowing ($\eta_h = 1$), i.e. the lower slot is closed. Figure 13 shows the evolutions of lift (a) and pitching moment (b) generation for a constant Coandă radius ($\frac{r}{c_{base}} = 0.02$) and different upper slot heights h_u when the plenum pressure ratio is increased, i.e. when the slot outflow velocity U_{jet} grows. As can be seen the jet velocity must exceed the free stream velocity U_∞ to produce significant lift and pitching moment increments. But thereafter effectiveness grows with the jet velocity ratio $\frac{U_{jet}}{U_\infty}$ in an approximately linear manner and the curve slopes become steeper with increasing slot height, i.e. increasing outflow momentum. However, they exhibit signs of saturation for larger slot sizes. The regression lines in Figure 14 confirm this behaviour for a variety of Coandă radii. Further opening of the slot might not lead to the desired gain of lift when the slot size has already exceeded reasonable margins. Finally Figure 15 depicts the lift production dependent on the outflow momentum flux coefficient c_μ. Lower slot heights exhibit a higher effectiveness for a given value of momentum

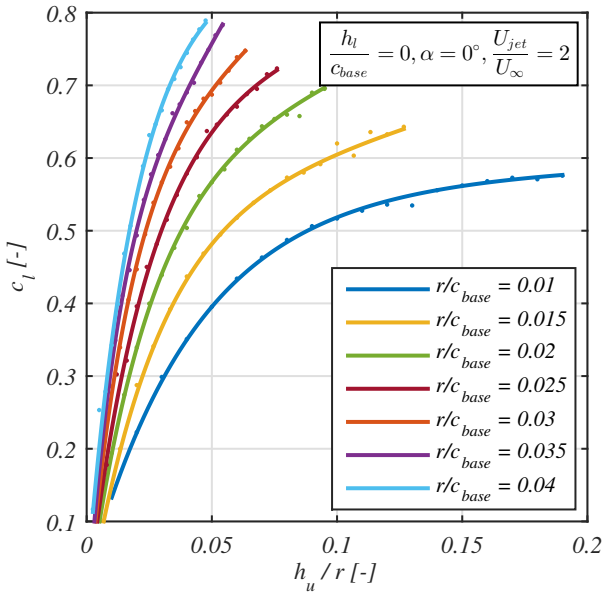

Fig. 14. Lift due to blowing through upper slot for different slot heights and Coandă radii (a) and momentum flux coefficient (b) ($\eta_h = 1$)

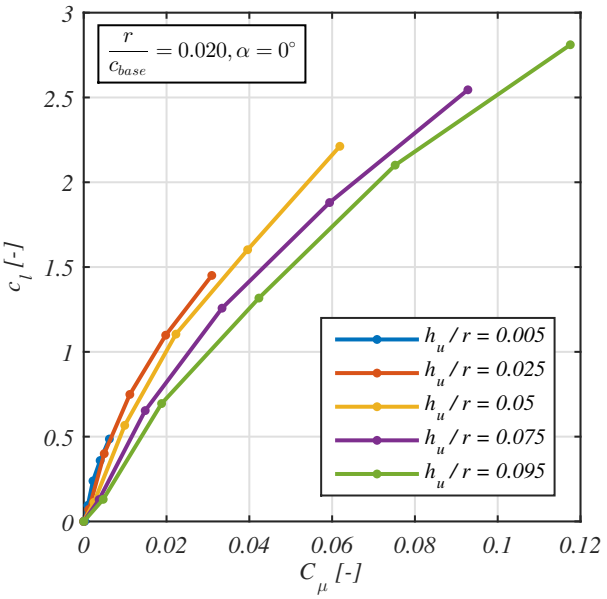

Fig. 15. Lift due to blowing through upper slot over momentum flux coefficient ($\eta_h = 1$)

flux that has to be provided by engine bleed air or by a decentralised compressor unit. However, smaller slot sizes more rapidly reach supersonic conditions with growing c_μ-values where expansion waves are prone to cause a premature jet sheet detachment at approx. $Ma_{jet} = 1.2$ followed by a stagnation or drop in lift production [23, 24, 25, 26, 27, 3]. Therefore smaller slot sizes are likely to limit the margins of potential lift generation. Note that the current calculations are restricted to maximum outflow velocities that respect the limits of the incompressible flow assumption ($Ma_{jet} \leq 1$) reasonably.

Asymmetric Blowing ($0 \leq \eta_h \leq 1$): For aircraft control purposes lift and pitching moment is meant to be controlled by adjusting both upper and lower slot independently to modify the rear stagnation point (see Figure 18). The geometrical configuration of the section can be described by the total slot height h_{total} and the ratio of upper and lower slot defined by the control parameter η_h. Given the pneumatic conditions, i.e. the total pressure inside the plenum, the jet outflow velocity ratio $\frac{U_{jet}}{U_\infty}$ is set for both slots. The total slot height h_{total} then determines the total jet mass flow. Figure 16 shows the lift and drag force as a function of η_h for different Coandă radii. Except at high slot ratio values η_h (where the lower slot is nearly closed) the lift coefficient exhibits an approximately linear behaviour for all Coandă radius to chord ratios $\frac{r}{c_{base}}$ when the control factor η_h increases. At $\eta_h = 1$ the simulation results show an enhanced lift production indicating that even low counter-pressures imposed by the lower jet cause premature detachment of the upper jet. Furthermore Coandă flap effectiveness ($\frac{\partial c_l}{\partial \eta_h}$) grows with increasing Coandă radius. However, the effectiveness gain seems to saturate at a radius to chord ratio of approx. $\frac{r}{c_{base}} = 0.02$. A more general illustration of this behaviour is provided by Figure 17. For a given Coandă radius the control force gain $\frac{\partial c_l}{\partial \eta_h}$ cannot be increased arbitrarily by opening both slots unboundedly. Hence, the total slot height h_{total} should be chosen inside reasonable margins relative to the Coandă radius. Furthermore, as can be seen in Figure 16b the aerofoil section drag decreases slightly until $\eta_h = 0.2$ before it disproportionately rises to its maximum value at $\eta_h = 1$. Generally drag grows with increasing Coandă radius. Note that the section drag coefficient c_d only includes the integrated friction and pressure forces acting on the aerofoil and Coandă surface skin. The thrust force effect through blowing is not added.

Dependency on angle of attack: In general, dependency of control effectiveness on angle of attack is low up to moderate α-values. Figure 19 shows the lift generation through single-slot-blowing for three different angles of attack. While lift increments are nearly identical for $\alpha = 0°$ and $\alpha = 5°$ lift production under strong blowing conditions seems to be limited at high angles of attack ($\alpha = 10°$). However, the lift coefficients still are substantially higher than the maximum lift coefficient of the unblown lift polar (see Figure 23a). The lift increase under double-slot-blowing exhibits a similar dependency (see Figure 20). Only at $\alpha = 10°$ the Coandă flap lift gain $\frac{\partial c_l}{\partial \eta_h}$ is slightly lower than for lower angles of attack. Note that circulation

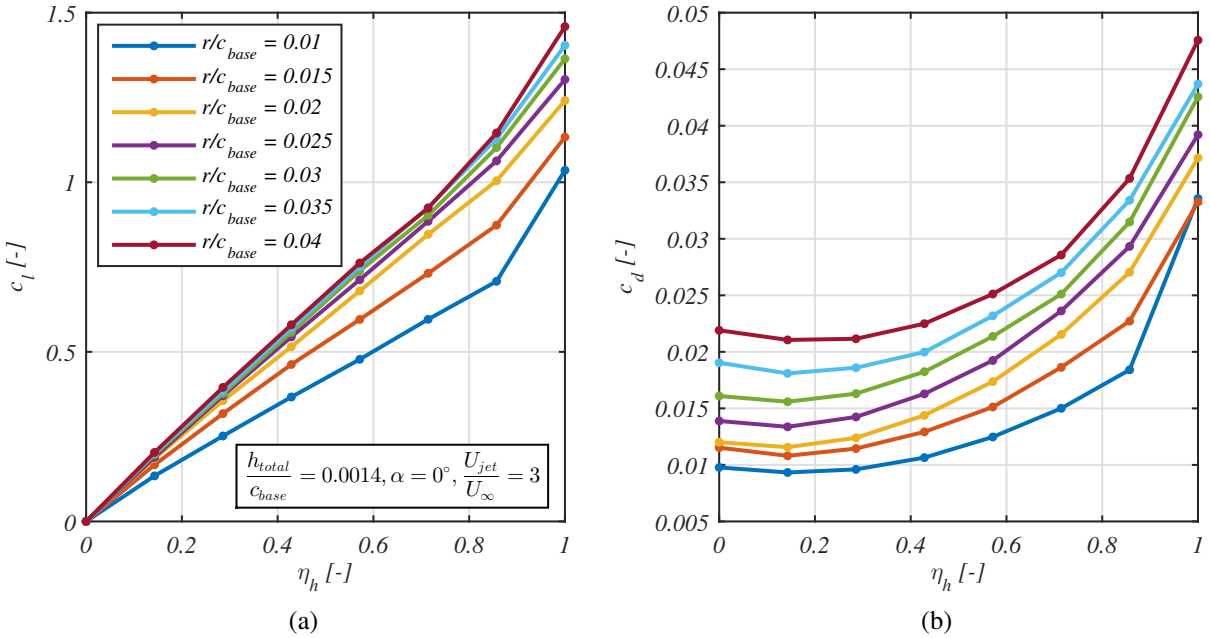

Fig. 16. Lift (a) and drag (b) due to double-slot-blowing for different Coandă radii

control aerofoils are prone to leading edge separation under high blowing conditions where high lift coefficients are obtained. Stall phenomena are still difficult to predict accurately by RANS calculations, especially under fully turbulent settings without transition model. Hence, the presented results are supposed to overestimate control effectiveness at high angles of attack.

Efficiency: Performance of a circulation control concept not only includes maximum effectiveness but also efficiency in terms of necessary resources, i.e. pressurised air. In this study the momentum flux coefficient c_μ is used as a measure of engine bleed air requirement. Figure 21 shows the regressed curves of lift augmentation $\frac{\partial c_l}{\partial c_\mu}$ in the single-slot-blowing case as a function of slot height at different blowing conditions. For a given Coandă radius ratio $\frac{r}{c_{base}}$ there is a blowing rate that provides a maximum in efficiency over the major range of slot heights (in this case $\frac{U_{jet}}{U_\infty} \approx 2$). Except at low blowing conditions ($\frac{U_{jet}}{U_\infty} \approx 1$) smaller slot sizes enable a more economic lift generation. Hence, it is recommended to chose the slot height ratio $\frac{h_u}{r}$ at reasonably low levels in order to maintain the required jet mass flow at low rates. Likewise it can be seen in Figure 22 that the ratio of Coandă flap effectiveness and momentum coefficient $\frac{\partial c_l/\partial \eta_h}{c_\mu}$ is higher for low total slot heights when the aerofoil is operated in the double-slot-blowing mode. The regression curves indicate that low Coandă radii with relatively large total slot heights can achieve higher efficiencies than large radii with relatively small slot heights.

Symmetric Blowing ($\eta_h = 0$): Of course, effectiveness and efficiency of the Coandă aerofoil is particularly important for flight phases where aircraft are facing high control moment requirements, e.g. during final approach. However, cruise phases span large portions of the design mission in most cases. To reduce base drag the working points of the Coandă flap system are likely to be chosen close to symmetric blowing operation ($\eta_h = 0$) rather than to shut off the active flow control system during cruise. Figure 23 shows the lift and drag characteristics of the aerofoil under symmetric blowing conditions. While caution is required for statements about the results in the stall region due to modelling capabilities the lift curves exhibit an interesting behaviour in the range of moderate angles of attack ($4° < \alpha < 9°$). Here, low blowing rates ($\frac{U_{jet}}{U_\infty} = 1$) appear to increase the lift coefficients and lift curve slopes whereas higher blowing rates ($\frac{U_{jet}}{U_\infty} > 1$) reduce lift compared to the unblown case ($\frac{U_{jet}}{U_\infty} = 0$). In contrast, high blowing rates are favourable in terms of drag as can be seen in Figure 23b. Again, the section drag coefficient c_d does not include the thrust force effect through blowing. The plotted drag values represent the base drag reduction due to separation control and subsequent generation of high pressure zones on the blunt trailing edge where both jets clash. Adding the propulsive effect of blowing would further decrease drag and would even lead to negative values, i.e. net thrust. However, this drag reduction must be traded off against the cost and penalties that affect the efficiency of the propulsion system and of the entire aircraft system.

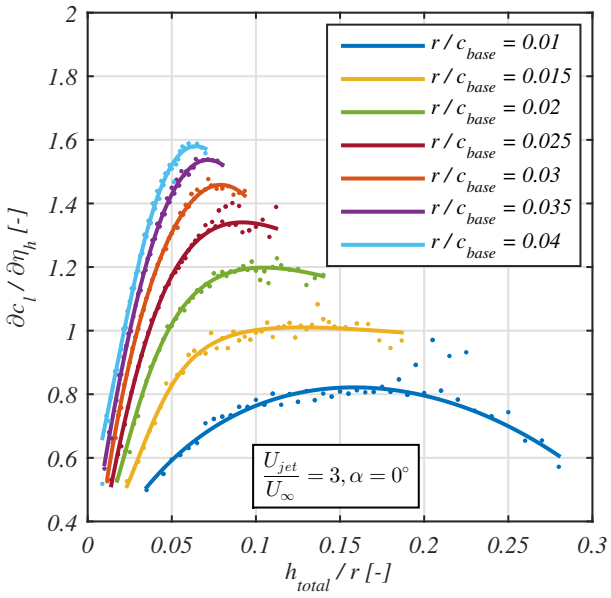

Fig. 17. Lift increase due to control parameter η_h for different total slot heights and Coandă radii

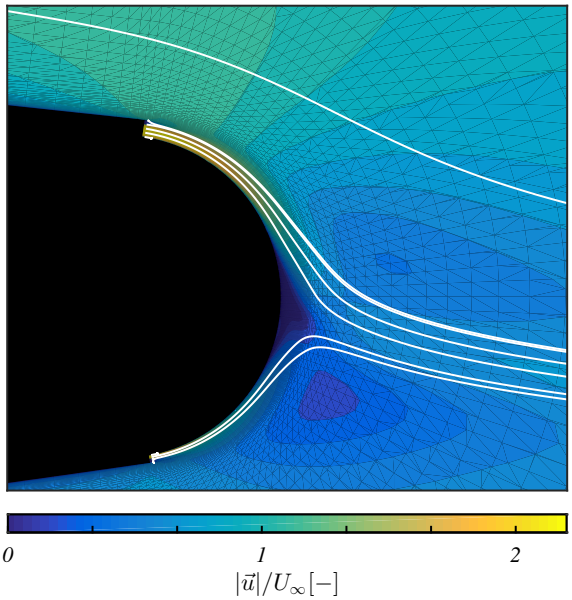

Fig. 18. Flow field at trailing edge under double-slot-blowing conditions

6 CONCLUSION

Two modifications of Menter's SST turbulence model have been presented aiming to increase robustness and accuracy for the preliminary design of active flow control systems. Reynolds-averaged Navier-Stokes simulations have been performed for a validation test case to assess the impact of each turbulence model modification. The introduction of modified formulations for both the blending function and SST formulation turned out to contribute to more robust and more accurate results up to high blowing conditions for the tested range.

The subsequent application of the presented RANS method in the context of a parametric study gave insight into the sensitivity of control effectiveness of a circulation control section based on the NACA-64A012 aerofoil. Results showed that the jet outflow velocity ratio must exceed a value of $\frac{U_{jet}}{U_\infty} = 1$ to achieve a significant gain in lift and pitching moment which then grows linearly with jet outflow velocity though. While increasing Coandă radii are favourable for achievable control forces inside the analysed ranges the lift increase through opening of the upper slot exhibits a saturated behaviour at larger slot sizes. In double-slot-blowing mode both lift and pitching moment coefficients exhibit an approximately linear behaviour with the jet outflow ratio η_h of upper and lower slot. The Coandă surface radius ratio $\frac{r}{c_{base}}$ as well as the total slot height h_{total} have significant impact on control effectiveness $\frac{\partial c_l}{\partial \eta_h}$, however, with saturation tendency at higher radius and slot sizes. Too large slot heights might even lead to reduced control moment generation. Moreover the dependency of control effectiveness on angle of attack revealed low up to moderate incidences. However, near stall the results indicated a reduced potential for lift generation under intensive blowing conditions. Furthermore the efficiency of control moment generation in terms of bleed air consumption has been investigated. Here, small slot sizes can reduce the required jet mass flow significantly and low Coandă radii with relatively large total slot heights can achieve higher efficiencies than large radii with relatively small slot heights. Finally a compromise has to be found when choosing a radius for the Coandă surface. Smaller radii might be more efficient but maximum attainable lift coefficients diminish with decreasing radii. Concerning aerodynamic performance of the Coandă flap system during cruise and loiter phases higher blowing rates ($\frac{U_{jet}}{U_\infty} > 1$) lead to a visibly negative impact on the lift polar, when symmetric blowing mode ($h_u = h_l$) is intended. However, symmetric blowing can reduce the natural base drag of large Coanda radii significantly. Here, a final statement about global system efficiency requires the consideration of the cost due to pressurised air supply (e.g. by engine bleed). The benefit or penalty of the Coandă flap system depends on the intended design mission of the aircraft. Therefore only a multidisciplinary examination of the individual flight states including aerodynamics, flight mechanics and propulsion will give insight into the overall performance of this fluidic flight control system for flapless flight.

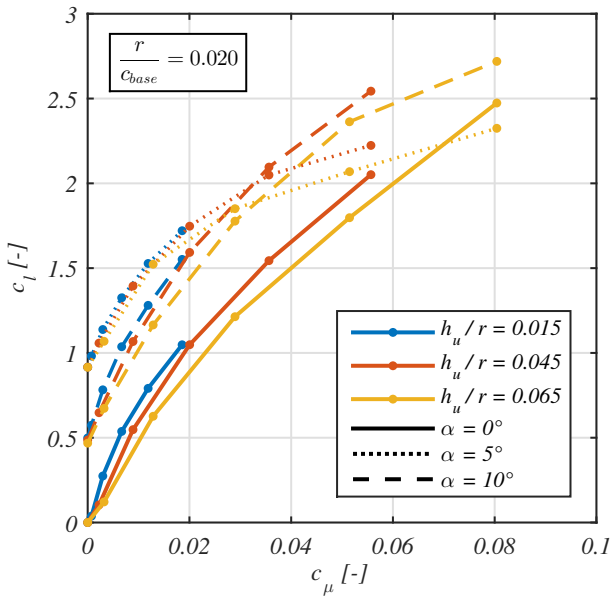

Fig. 19. Dependency of lift generation on angle of attack

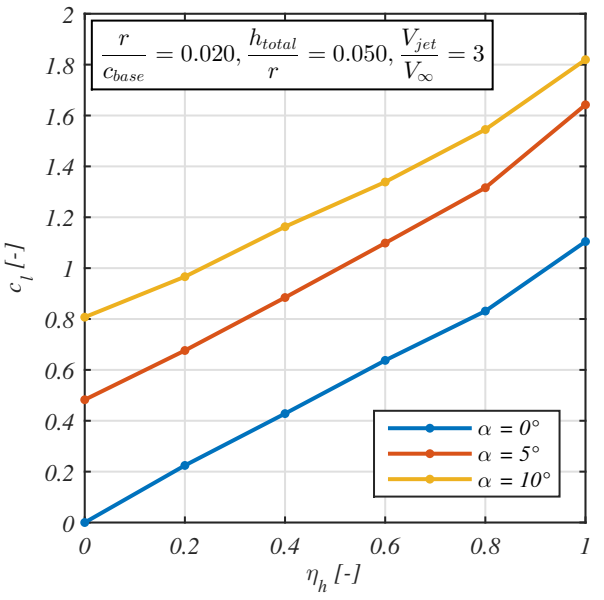

Fig. 20. Dependency of lift of Coandă flap effectiveness on angle of attack

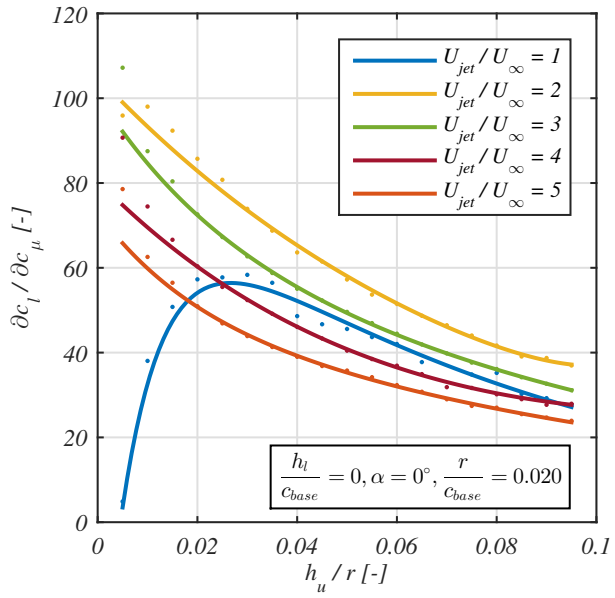

Fig. 21. Dependency of lift augmentation on slot height and blowing conditions ($\eta_h = 1$)

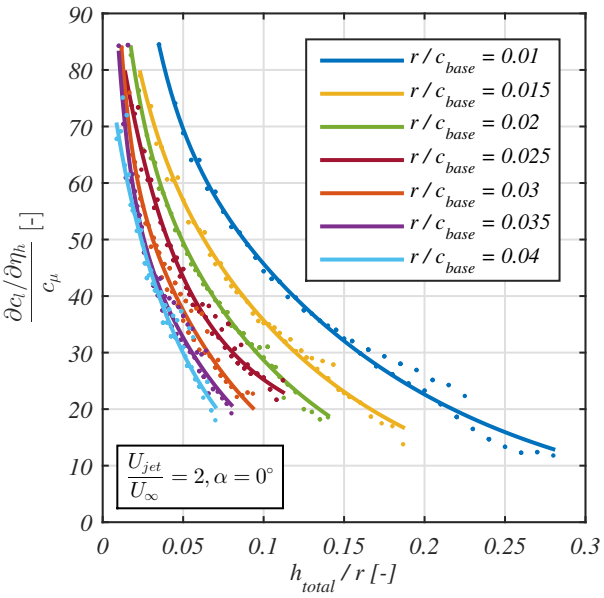

Fig. 22. Ratio of Coandă flap effectiveness and momentum coefficient for different slot heights and Coandă radii

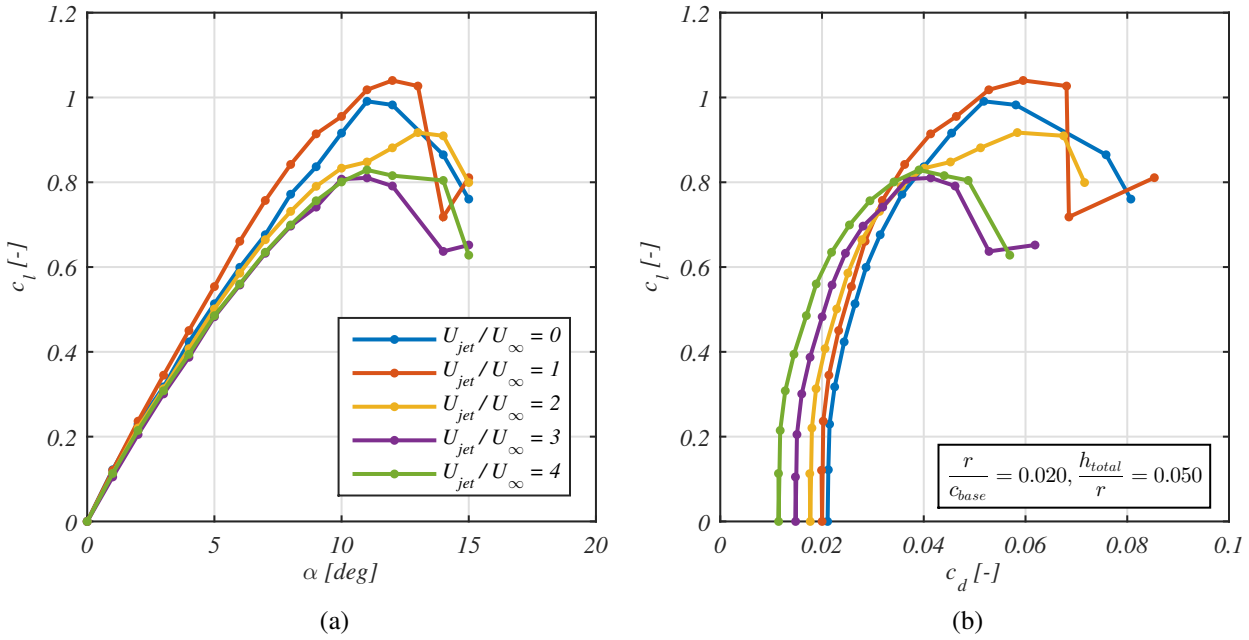

Fig. 23. Lift (a) and drag (b) polar for different symmetric blowing conditions ($\eta_h = 0$)

References

[1] J. Abramson. Characteristics of a Cambered Circulation Control Airfoil Having Both Upper and Lower Surface Trailing Edge Slots. Technical report, Naval Surface Warfare Center, Carderock Division, West Bethesda, 2004.

[2] S. Frith and N. Wood. Investigation of Dual Circulation Control Surfaces for Flight Control. In *2nd AIAA Flow Control Conference*, Fluid Dynamics and Co-located Conferences. American Institute of Aeronautics and Astronautics, 2004.

[3] M. G. Alexander, S. G. Anders, S. K. Johnson, J. P. Florance, and D. F. Keller. Trailing Edge Blowing on a Two-Dimensional Six-Percent Thick Elliptical Circulation Control Airfoil Up to Transonic Conditions: NASA/TM-2005-213545. Technical report, NASA Langley Research Center, Langley, USA, 2005.

[4] G. Jones, C.-S. Yao, and B. Allan. Experimental Investigation of a 2D Supercritical Circulation-Control Airfoil Using Particle Image Velocimetry. In *3rd AIAA Flow Control Conference*, Fluid Dynamics and Co-located Conferences. American Institute of Aeronautics and Astronautics, 2006.

[5] R. Englar, G. Jones, B. Allan, and J. Lin. 2-D Circulation Control Airfoil Benchmark Experiments Intended for CFD Code Validation. In *47th AIAA Aerospace Sciences Meeting including The New Horizons Forum and Aerospace Exposition*, Aerospace Sciences Meetings. American Institute of Aeronautics and Astronautics, 2009.

[6] R. C. Swanson and C. L. Rumsey. Computation of circulation control airfoil flows. *Computers & Fluids*, 38(10):1925–1942, 2009.

[7] B. Allan, G. Jones, and J. Lin. Reynolds-Averaged Navier-Stokes Simulation of a 2-D Circulation Control Wind Tunnel Experiment. In *49th AIAA Aerospace Sciences Meeting including the New Horizons Forum and Aerospace Exposition*, Aerospace Sciences Meetings. American Institute of Aeronautics and Astronautics, 2011.

[8] K. Stadlberger and M. Hornung. Aerodynamic Modelling of an Active Flow Control System for Flapless Flight Control in the Preliminary Design Stages. In *5th CEAS Air & Space Conference*, 2015.

[9] W. Baker and E. Paterson. RANS CFD Simulation of a Circulation-Control Foil: Validation of Performance, Flow Feild, and Wall Jet. In *3rd AIAA Flow Control Conference*, Fluid Dynamics and Co-located Conferences. American Institute of Aeronautics and Astronautics, 2006.

[10] H. F. Fasel, A. Gross, and S. Wernz. Investigation of Turbulent Coanda Wall Jets Using DNS and RANS. In *Applications of Circulation Control Technology*, Progress in Astronautics and Aeronautics, pages 401–420. American Institute of Aeronautics and Astronautics, 2006.

[11] R. C. Swanson, C. L. Rumsey, and S. G. Anders. Aspects of Numerical Simulation of Circulation Control Airfoils. In *Applications of Circulation Control Technology*, Progress in Astronautics and Aeronautics, pages 469–498. American Institute of Aeronautics and Astronautics, 2006.

[12] A. Zacharos and K. Kontis. Numerical Studies on an Active Flow Circulation Controlled Flap Concept for Aeronautical Applications. *Transactions of the Japan Society for Aeronautical and Space Sciences*, 49(163):25–30, 2006.

[13] P. A. Chang, J. Slomski, T. Marino, M. P. Ebert, and J. Abramson. Full Reynolds-Stress Modeling of Circulation Control Airfoils. In *Applications of Circulation Control Technology*, Progress in Astronautics and Aeronautics, pages 445–468. American Institute of Aeronautics and Astronautics, 2006.

[14] K. Stadlberger and M. Hornung. Challenges in the Modelling of Blown Circulation Control Aerofoils. In *63. Deutscher Luft- und Raumfahrtkongress der Deutschen Gesellschaft für Luft- und Raumfahrt e.V.*, 2014.

[15] F. R. Menter, M. Kuntz, and R. Langtry. Ten Years of Industrial Experience with the SST Turbulence Model. *Turbulence, Heat and Mass Transfer*, (4):625–632, 2003.

[16] C. L. Rumsey and T. Nishino. Numerical study comparing RANS and LES approaches on a circulation control airfoil. *International Journal of Heat and Fluid Flow*, 32(5):847–864, 2011.

[17] D. B. Spalding. A novel finite difference formulation for differential expressions involving both first and second derivatives. *International Journal for Numerical Methods in Engineering*, 4(4):551–559, 1972.

[18] F. H. Harlow and J. E. Welch. Numerical Calculation of Time–Dependent Viscous Incompressible Flow of Fluid with Free Surface. *Physics of Fluids (1958-1988)*, 8(12):2182–2189, 1965.

[19] F. R. Menter. Two-equation eddy-viscosity turbulence models for engineering applications. *AIAA Journal*, 32(8):1598–1605, 1994.

[20] A. Hellsten. Some improvements in Menter's k-omega SST turbulence model. In *29th AIAA, Fluid Dynamics Conference*, Fluid Dynamics and Co-located Conferences. American Institute of Aeronautics and Astronautics, 1998.

[21] P. R. Spalart and M. Shur. On the sensitization of turbulence models to rotation and curvature. *Aerospace Science and Technology*, 1(5):297–302, 1997.

[22] R. Swanson, C. Rumsey, and S. Anders. Progress Towards Computational Method for Circulation Control Airfoils. In *43rd AIAA Aerospace Sciences Meeting and Exhibit*, Aerospace Sciences Meetings. American Institute of Aeronautics and Astronautics, 2005.

[23] R. J. Englar. Two-Dimensional Transonic Wind Tunnel Tests of Three 15-Percent Thick Circulation Control Airfoils. Technical Report AD882075, David W. Taylor Naval Ship Research and Development Center, 1970.

[24] R. J. Englar. Two-Dimensional Subsonic Wind Tunnel Tests of Two 15-Percent Thick Circulation Control Airfoils. Technical report, David W. Taylor Naval Ship Research and Development Center, 1971.

[25] R. J. Englar. Two-Dimensional Subsonic Wind Tunnel Tests of a 30-Percent Thick Circulation Control Airfoil. Technical report, David W. Taylor Naval Ship Research and Development Center, 1972.

[26] R. J. Englar. Experimental Investigation of the High Velocity Coanda Wall Jet Applied to Bluff Trailing Edge Circulation Control Airfoils. Technical report, David W. Taylor Naval Ship Research and Development Center, Bethesda and Maryland and USA, 1975.

[27] K. C. Cornelius and G. A. Lucius. Physics of Coanda jet detachment at high-pressure ratio. *Journal of Aircraft*, 31(3):591–596, 1994.